

Empirical Calibration of Na I D and Other Absorption Lines as Tracers of High-Redshift Neutral Outflows

Lorenzo Moretti¹, Sirio Belli¹, Gwen C. Rudie², Andrew B. Newman², Minjung Park³, Amir H. Khoram^{1,4}, Nima Chartab⁵, Darko Donevski^{6,7}

¹ Dipartimento di Fisica e Astronomia, Università di Bologna, Bologna, Italy

² The Observatories of the Carnegie Institution for Science, Pasadena, CA, USA

³ Center for Astrophysics | Harvard & Smithsonian, Cambridge, MA, USA

⁴ INAF, Astrophysics and Space Science Observatory, Bologna, Italy

⁵ Caltech/IPAC, Pasadena, CA, USA

⁶ National Centre for Nuclear Research, Warsaw, Poland

⁷ SISSA, Trieste, Italy

July 11, 2025

ABSTRACT

Recent JWST observations of massive galaxies at $z > 2$ have detected blueshifted absorption in Na I D and other resonant absorption lines, indicative of strong gas outflows in the neutral phase. However, the measured mass outflow rates are highly uncertain because JWST observations can only probe the column density of trace elements such as sodium, while most of the gas is in the form of hydrogen. The conversion between the column density of sodium and that of hydrogen is based on observations of gas clouds within the Milky Way, and has not been directly tested for massive galaxies at high redshift. In order to test this conversion, we study a unique system consisting of a massive quiescent galaxy (J1439B) at $z = 2.4189$ located at a projected distance of 38 physical kpc from the bright background quasar QSO J1439+1117. The neutral outflow from the galaxy is observed as a sub-damped Lyman- α absorber (sub-DLA) in the spectrum of the background quasar, which enables a direct measurement of the hydrogen column density from Lyman transitions. We obtain new near-infrared spectroscopy with Magellan/FIRE and detect Na I D and other resonant absorption lines from Mg II, Mg I, and Fe II. We are thus able to derive new, empirical calibrations between the column density of trace elements and the hydrogen column density, that can be used to estimate the mass and the rate of neutral gas outflows in other massive quiescent galaxies at high redshift. The calibration we derive for Na I is only 30% lower than the local relation that is typically assumed at high redshift, confirming that the neutral outflows observed with JWST at $z > 2$ are able to remove a large amount of gas and are thus likely to play a key role in galaxy quenching. However, using the local calibration for Mg II yields an order-of-magnitude discrepancy compared to the empirical calibration, possibly because of variations in the dust depletion.

Key words. Galaxies: evolution – Galaxies: high-redshift – Quasars: absorption lines

1. Introduction

Gas outflows play a crucial role in galaxy formation and evolution, and may be responsible for shutting down star formation in massive systems. However, direct observational evidence for a major impact of outflows on the star formation history of massive galaxies has been difficult to obtain, partly because the multiphase nature of galaxy outflows makes it challenging to measure the total amount of mass ejected (Förster Schreiber & Wuyts 2020; Veilleux et al. 2020). This observational challenge is one of the main obstacles in the search for a direct link between AGN-driven outflows and galaxy quenching (e.g., Harrison 2017; Ciccone et al. 2018).

At $z \sim 2$, when massive galaxies start entering the quenching phase in large numbers, observational studies have been able to identify the widespread presence of ionized outflows, which can be detected via strong emission lines (e.g., Förster Schreiber et al. 2014); however, the corresponding mass outflow rates are low, meaning that ionized outflows are unlikely to shut off star formation and cause galaxy quenching (e.g., Lamperti et al. 2021; Concas et al. 2022). On the other hand, most of the outflow mass is expected to be in the cold phase (Veilleux et al. 2020), which is particularly difficult to detect at high red-

shift. Sub-millimeter observations probe cold molecular gas, but detecting outflows in normal galaxies (as opposed to quasars) with this method is challenging (e.g., Herrera-Camus et al. 2019; Spilker et al. 2020; Barfety et al. 2025). Alternatively, metal absorption lines in the rest-frame optical or UV can be used to trace the neutral atomic phase. This technique has been successfully used in the local and low-redshift universe (e.g., Rupke et al. 2005; Tremonti et al. 2007), but requires a high signal-to-noise ratio on the galaxy continuum emission, which until recently was out of reach for galaxies at $z > 1$ without resorting to stacking (Steidel et al. 2010; Maltby et al. 2019; Taylor et al. 2024) or strong gravitational lensing (Pettini et al. 2002; Jafarizadeh et al. 2020; Man et al. 2021).

The advent of JWST has enabled a major step forward in the field, making it possible to detect metal absorption lines due to neutral atomic gas in high-redshift galaxies. The neutral gas measurements are typically obtained from the Na I D doublet (Davies et al. 2024; Belli et al. 2024; D'Eugenio et al. 2024; Sun et al. 2025), but also Ca, Mg, and Fe absorption lines have been used (Liboni et al. 2025; Wu 2025; Valentino et al. 2025). By measuring the mass and kinematics of the dense, neutral gas phase, these studies conclude that outflows observed in massive

galaxies are able to remove the majority of the gas reservoir, thus leading to galaxy quenching. However, these early results are affected by strong systematics, leading to an order-of-magnitude uncertainty on the measured mass outflow rate (Belli et al. 2024). The major source of uncertainty comes from the fact that observations can only probe a trace element such as sodium, while most of the mass is in the form of hydrogen. A conversion of the observed column density $N_{X,i}$ (i.e., of element X in the i -th ionization stage) to the column density of neutral hydrogen N_{HI} is thus needed. The conversion can be written as (e.g. Rupke et al. 2005):

$$N_{\text{HI}} = \frac{N_{X,i}}{(n_{X,i}/n_X) \cdot 10^{[X/H]} (n_X/n_H)_\odot 10^{\delta_X}}. \quad (1)$$

This calibration requires knowledge of three different physical quantities: the ionization fraction ($n_{X,i}/n_X$), the depletion onto dust δ_X , and the elemental abundance in the gas, which is written as the product of the abundance relative to solar, $10^{[X/H]}$, by the abundance in the Sun, $(n_X/n_H)_\odot$. These properties can be accurately measured in regions within the Milky Way, and the local values are adopted when studying extragalactic systems. For example, common assumptions for Na I are $(n_{\text{Na I}}/n_{\text{Na}}) = 0.1$ (meaning that only 10% of the sodium is in the neutral phase) and $\delta_{\text{Na}} = -0.95$, together with $\log(n_{\text{Na}}/n_H)_\odot = -5.69$ (Savage & Sembach 1996; Rupke et al. 2005). The abundance of sodium in the outflow is rarely measured, and for massive galaxies it is often assumed that $[\text{Na}/\text{H}] = 0$, i.e. the gas has solar abundance. With these assumptions, the Na-to-H conversion becomes

$$\log N_{\text{HI}} = \log N_{\text{Na I}} + 7.64. \quad (2)$$

There are several limitations with the calibration discussed above. First, variations in dust depletion, ionization correction, and metal abundance along different lines of sight in the Milky Way can lead to differences in the calibration by up to an order of magnitude (Rupke et al. 2002). Second, it is expected that the physical conditions in large-scale outflows at high redshift are substantially different compared to those in the Milky Way due to, for example, the presence of shocks, photoionization by AGN, and potentially different dust composition.

In the present study we address these limitations by directly measuring the column density for both sodium and hydrogen in the large-scale outflow near J1439B, a massive quiescent galaxy at $z = 2.4189$ (Rudie et al. 2017). This is possible because of the chance alignment between the galaxy outflow and a background quasar, which emits a strong, continuous spectrum extending into the rest-frame UV. Analysis of the Lyman absorption lines in high-resolution optical spectroscopy provides accurate measurements of the H I column density (Srianand et al. 2008; Noterdaeme et al. 2008); we obtained new near-infrared spectroscopy with Magellan/FIRE to measure Na I D and other resonant absorption lines. By circumventing the assumptions needed by previous methods, we provide an empirical, direct calibration of Na I, Mg I, Mg II, and Fe II as tracers of hydrogen in neutral outflows. The nature of the galaxy and of its outflow, which is likely driven by an AGN, makes this calibration particularly suited to the study of galaxy quenching at high redshift.

In Section 2 we review the physical properties of the system known from previous studies, and perform a fit to the broadband photometry of the galaxy to estimate its properties. In Section 3 we introduce new near-infrared spectroscopic data and describe the equivalent width measurements. In Section 4 we provide empirical calibrations for Na I, Mg II, Mg I, and Fe II. Finally, we summarize and discuss our results in Section 5.

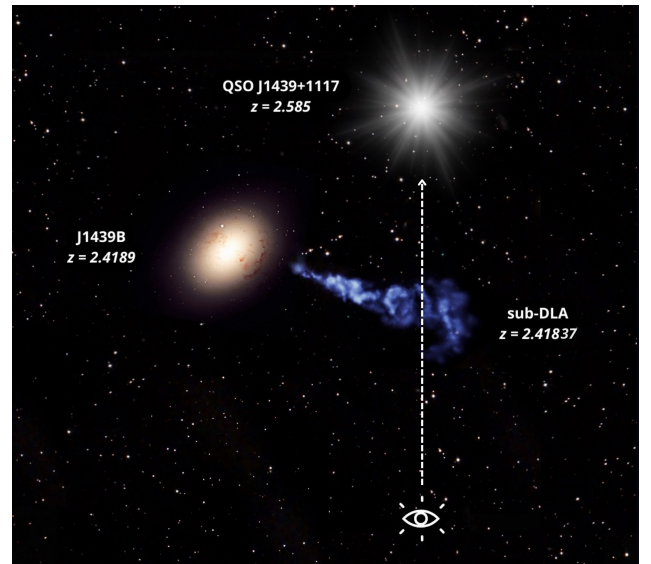


Fig. 1. Artistic illustration of the system, consisting of the galaxy J1439B and its outflow, detected as a sub-DLA in the spectrum of the background quasar J1439+1117.

2. The System

The unique system studied in this work consists of J1439B, a massive galaxy at $z = 2.4189$, and a sub-damped Lyman- α absorber (sub-DLA) at roughly the same redshift, seen in the spectrum of the background quasar QSO J1439+1117. The separation between the galaxy and the QSO line of sight is $4''.7$, corresponding to 38 physical kpc at the galaxy redshift. The proximity to the galaxy, the peculiarly high metallicity, and the presence of molecular gas point to the identification of the sub-DLA with the cold outflow ejected by J1439B, as argued in detail by Rudie et al. (2017). An illustration of the system geometry is shown in Figure 1.

2.1. The Outflow

The outflow of J1439B was first discovered as a $z = 2.41837$ absorber in the spectrum of QSO J1439+1117 by Srianand et al. (2008) and Noterdaeme et al. (2008), who characterized its physical properties using a high-resolution VLT/UVES spectrum. Analysis of the Ly- α damping wings and of the Ly- β and Ly- γ absorption lines yield a column density of neutral hydrogen of $\log N_{\text{HI}} = 20.1 \pm 0.1$, which is just short of the classical DLA threshold ($\log N_{\text{HI}} > 20.3$). Four additional components are detected, with velocities in the range 0 to -1000 km/s and column densities a factor of at least 5 smaller compared to the main absorber.

What makes this sub-DLA particularly interesting is its high chemical enrichment, with a roughly solar metallicity, and the detection of molecular gas through CO absorption lines, with a molecular fraction $f = 2N_{\text{H}_2}/(N_{\text{HI}} + 2N_{\text{H}_2}) = 0.27 \pm 0.10$ (Srianand et al. 2008). These properties are highly unusual for a DLA or sub-DLA system, but are in line with expectations for gas outflowing from a massive, evolved galaxy.

2.2. The Galaxy

The galaxy J1439B was discovered and analyzed by Rudie et al. (2017) when looking for possible counterparts to the sub-DLA at $z = 2.41837$. A near-infrared spectrum of the galaxy, obtained

with Magellan/FIRE, reveals $H\alpha$, $H\beta$, $[N\ II]$ and $[O\ III]$ emission lines at a redshift $z = 2.4189$, corresponding to a separation from the main sub-DLA component of 47 km/s along the line-of-sight. The line ratios are inconsistent with ionization by young stars, and lie in the AGN region of the BPT diagram (Baldwin et al. 1981). Moreover, the relatively large velocity dispersion in the forbidden line $[O\ III]$ suggests the presence of an ionized outflow, likely driven by AGN activity.

Rudie et al. (2017) also obtained broad-band photometry of J1439B in seven optical and near-infrared bands using the Magellan telescopes. Fitting the spectral energy distribution (SED) with FAST (Kriek et al. 2009) under the assumption of an exponentially declining star formation history yields a young, massive galaxy ($\log M_*/M_\odot = 10.7$) with relatively low star formation rate ($SFR = 7^{+17}_{-4} M_\odot \text{ yr}^{-1}$), which places J1439B about 0.7 dex below the main sequence of star formation (e.g., Shivaee et al. 2015; Leja et al. 2022).

2.3. Prospector Fit to the Broadband Photometry

In order to further constrain the physical properties of galaxy J1439B, we perform a new SED fit of the photometric measurements provided by Rudie et al.. We use the Prospector code (Johnson et al. 2021), which employs a substantially more flexible model compared to FAST, thus leading to more accurate results and realistic uncertainties.

The galaxy emission is modeled using a non-parametric star formation history with 14 time bins, adopting a continuity prior to ensure smooth transitions between adjacent time bins (Leja et al. 2019). The stellar templates are taken from the Flexible Stellar Population Synthesis (FSPS, Conroy et al. 2009; Conroy & Gunn 2010), assuming a Chabrier (2003) initial mass function (IMF), with the redshift fixed to the spectroscopic value. The model also includes parameters for metallicity and dust attenuation, which is treated using the parametrization of Kriek & Conroy (2013). The attenuation A_V and the ratio of diffuse-to-birth-cloud dust are left free, while the dust extinction index, which quantifies deviations from the canonical Calzetti et al. (2000) extinction law, was fixed to 0. This choice is supported by a recent study of massive quiescent galaxies with deep JWST spectroscopy (Park et al. 2024). Contributions from dust emission, nebular emission, and active galactic nuclei are not included in the model.

To account for potential systematics, we add in quadrature a 5% uncertainty to the photometric error, and include the fraction of possible photometric outliers as a free parameter in Prospector. The SED fitting was performed using the nested sampling method from the dynesty package (Speagle 2020). The best-fit SED model, evaluated at the maximum a posteriori (MAP) point in parameter space, fits well the observed broadband photometry, as shown in Figure 2.

The Prospector fit yields $\log M_*/M_\odot = 10.9 \pm 0.2$, $\log SFR/(M_\odot \text{ yr}^{-1}) = 1.2 \pm 0.8$, and $A_V = 0.6 \pm 0.4$. These results are in broad agreement with those obtained by Rudie et al. (2017) using FAST, but with a much larger uncertainty on the measured parameters. The best-fit star formation history presents a decline over the last Gyr, suggesting a recent quenching phase, but the posterior distribution encompasses a large range of shapes and normalizations. We conclude that the available photometry for J1439B is insufficient for a robust measurement of the star formation history. However, the quiescent nature of the galaxy is independently confirmed by the FIRE spectrum obtained by Rudie et al. (2017): the observed $H\alpha$ luminosity, which is certainly contaminated by AGN emission, gives an up-

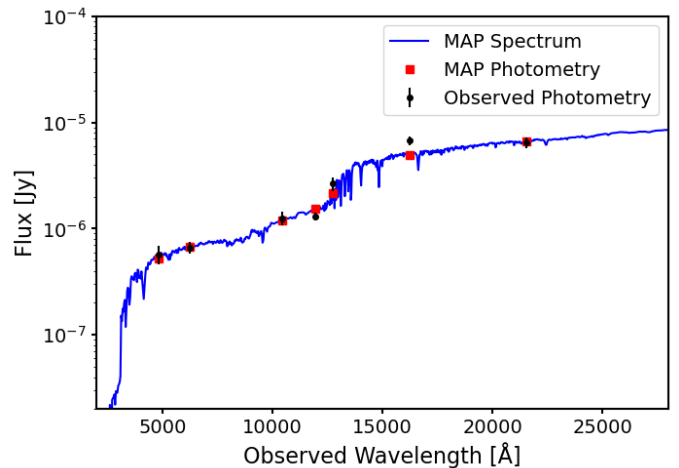


Fig. 2. SED fit to the broadband photometry of galaxy J1439B. The blue line represents the model spectrum, red squares represent the best-fit model photometry, and black circles with error bars indicate the observed photometry.

per limit of $SFR < 13 M_\odot/\text{yr}$ using the Kennicutt (1998) calibration converted to a Chabrier IMF. The SFR estimate accounts for dust attenuation derived from the observed Balmer decrement, which is fully consistent with the best-fit value of A_V obtained with Prospector.

3. Absorption Line Measurements

3.1. Spectroscopic Data

We observed QSO J1439+1117 with the Folded-port InfraRed Echellette (FIRE) spectrograph on the Baade Magellan Telescope in Chile. FIRE is a near-infrared, cross-dispersed echelle spectrograph providing medium-resolution spectroscopy over the full near-infrared range, 0.8–2.5 μm . Observations were conducted on March 9–10, 2024, using a $6'' \times 0.6''$ slit, yielding a spectral resolution $R \sim 6,000$. We adopted an AB dithering pattern with 20-minute exposures offset by $3''$. The total exposure time was 160 minutes under good weather conditions, with $0.6''$ seeing in the near-infrared. The observations were reduced with the FIREHOSE pipeline (Gagné et al. 2015), which includes flat-fielding, wavelength calibration, illumination correction, and slit tilt correction. We also observed an A0V star close to the target, and used its spectrum to perform the telluric correction using the *xtellcorr* package (Vacca et al. 2003). After extracting the 1D spectrum for each of the A and B nod positions, we detected a spurious absorption feature in the source spectrum at 20148.7 Å, close to the Na D doublet. This is due to a detector defect that lies near the source spectrum only in the A position. When combining the A-B and B-A spectra, we thus leave out the A-B spectrum in the region around Na D, obtaining a combined spectrum that has half the exposure time but is free from artifacts. The final 1D spectrum is shown in Figure 3 and is made publicly available¹. We note the presence of both emission lines from the QSO at $z = 2.585$ and absorption lines from the sub-DLA at $z = 2.41837$.

This system has also been previously observed in the optical by Srianand et al. (2008) and Noterdaeme et al. (2008) using the Ultraviolet and Visual Echelle Spectrograph (UVES) on the Very Large Telescope (VLT), under ESO program 278.A-5062(A).

¹ <https://doi.org/10.5281/zenodo.15237852>

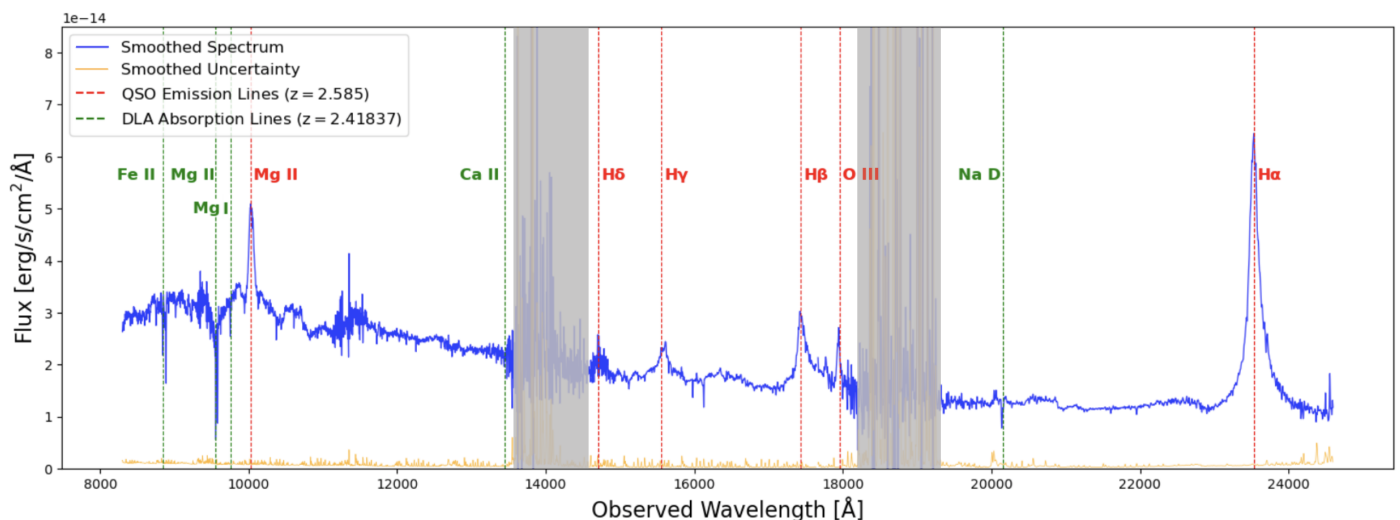


Fig. 3. *Magellan*/FIRE spectrum of QSO J1439+1117 (in blue; smoothed with a 4-pixel Gaussian kernel) and spectral uncertainty (in orange). Red dashed lines mark the main emission lines from the QSO at $z = 2.585$, while green dashed lines mark absorption lines from the sub-DLA at $z = 2.41837$.

The UVES spectrum covers the 3300–7100 Å range with a resolving power of $R = 50,000$. We use this high-resolution spectrum only for visualization purposes. We adopt the hydrogen column densities measured from the UVES data for each velocity component by [Srianand et al. \(2008\)](#).

3.2. Equivalent Width Measurements

In the FIRE spectrum we identify several resonant absorption lines due to cold gas: Fe II 2586, 2600, Mg II 2796, 2803, Mg I 2853, and Na I 5891, 5897 (the Na I D doublet). These are shown in Figure 4, plotted with respect to the systemic redshift of the J1439B galaxy, and with the spectral continuum normalized to a value of 1 in each region. We also look for the Ca II 3934, 3969 doublet (Ca II H and K lines), but at the sub-DLA redshift these wavelengths fall into a region with very low atmospheric transmission, making it impossible to detect any absorption. In the bottom of Figure 4 we also show a select sample of transitions in the rest-frame UV from the UVES spectrum: O I 1302, Fe II 1608 and Al II 1670. Vertical dashed lines identify four velocity components for which [Srianand et al.](#) and [Noterdaeme et al.](#) measure the H I column density from Voigt fits to the Lyman absorption lines. These components are found at –640, –428, –164, and –47 km/s compared to the galaxy systemic redshift. A fifth component at –938 km/s is much weaker than the others and falls outside of the velocity range shown in the figure.

The kinematic structure of the sub-DLA in the high-resolution UVES spectrum appears complex, with the outflow consisting of multiple cloudlets, each traveling at a different velocity, as indicated by the presence of distinct absorption profiles of the same element at varying velocities. All absorption lines are blueshifted by several tens to hundreds of kilometers per second — clear evidence of a neutral outflow moving toward the observer. The absorption lines in the FIRE spectrum are aligned with the strongest velocity components, but appear broader due to the lower spectral resolution. Moreover, for the Mg II and Fe II lines, saturated absorption causes blending between the main component of the sub-DLA at –47 km/s and the adjacent component at –164 km/s, similarly to what is observed for O I in the UVES spectrum.

We measure the equivalent width EW of each transition in the FIRE spectrum in order to quantify the strength of the absorption. For Mg I and Na I we integrate the spectrum only in the wavelength region corresponding to the strongest velocity component at –47 km/s (blue shaded areas in Figure 4); while for Mg II and Fe II we measure the combined EW of the –47 km/s and –164 km/s components, which are blended (red shaded areas in the figure). All EW measurements are reported in Appendix A.

4. Column Density Calibrations

To convert the measured EW of metal lines to column density values we make use of the linear relation valid in the optically thin regime (e.g., [Draine 2011](#)):

$$EW = \frac{\pi e^2}{m_e c^2} \lambda_0^2 N f \simeq (8.85 \cdot 10^{-13} \text{ cm}) \lambda_0^2 N f, \quad (3)$$

where λ_0 is the restframe wavelength of the transition and f is its oscillator strength. When the regime becomes optically thick, then the same observed EW corresponds to a higher number of atoms, and this relation can only provide a lower limit on the column density. The doublet ratio can be used to discriminate between the two regimes: in the optically thin case the doublet ratio is roughly equal to the ratio of the oscillator strengths, while in the optically thick case the absorption lines become saturated, and the doublet ratio becomes closer to 1. Measurements of doublet ratios and column densities are reported in Appendix A.

4.1. Sodium

The doublet ratio for Na I, measured for the –47 km/s velocity component, is consistent with the theoretical value of ~ 2 and indicates that the absorption is optically thin. We can thus derive a robust measurement of the Na I column density (see Table A.1). Comparing this to the H I column density for the same velocity component, we obtain a column density ratio $\log(N_{\text{H I}}/N_{\text{Na I}}) = 7.5 \pm 0.1$. Assuming a linear relation between the hydrogen and the neutral sodium column density, we use this result to derive an empirical calibration that can be used to infer

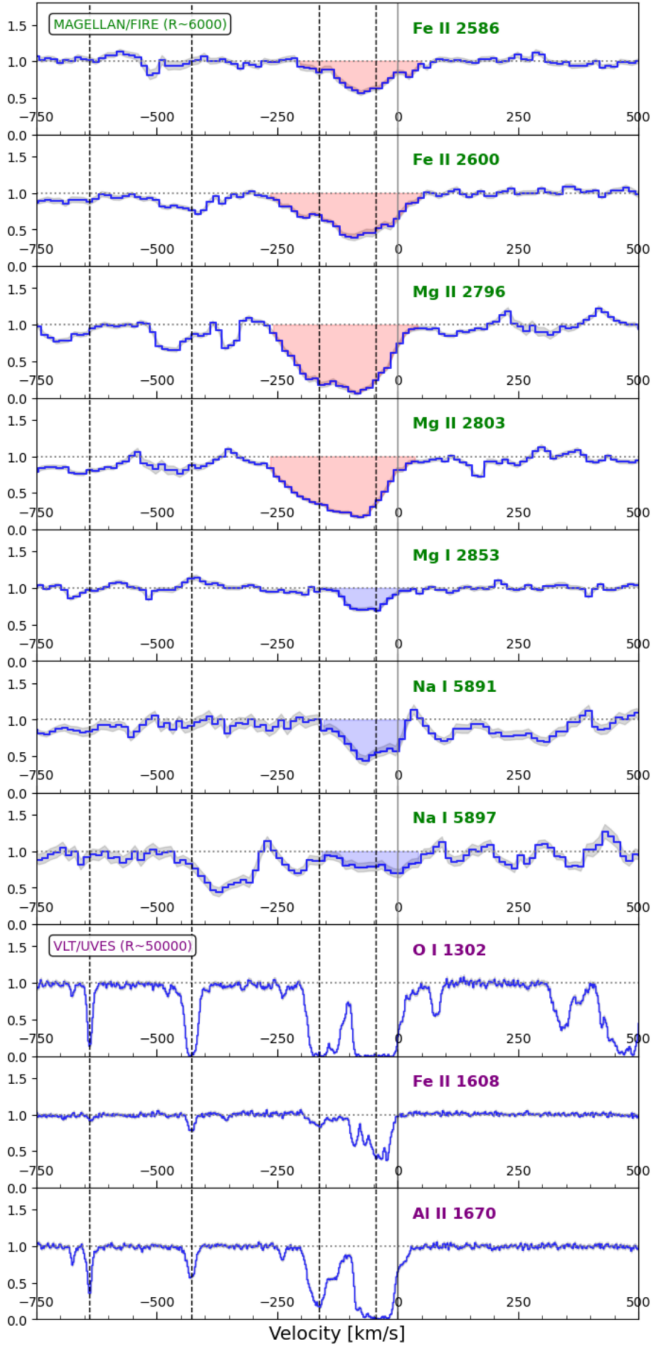


Fig. 4. Absorption features in the QSO J1439+1117 spectrum in velocity space, with zero corresponding to the systemic velocity of galaxy J1439B. Normalized flux is shown on the y-axis of each panel. The top panels show Fe II, Mg II, Mg I and Na I transitions in the FIRE spectrum. The shaded areas represent the spectral regions used in the calculation of the EW for the component at -47 km/s (blue shaded areas), or for the sum of the components at -47 and -164 km/s when they are blended (red shaded areas). The bottom panels show O I, Fe II, and Al II in the higher-resolution UVES data. Vertical dashed lines mark the absorbers used to fit the H I distribution in [Srianand et al.](#) and [Nozdaeme et al.](#).

the hydrogen mass from the observed Na I absorption in other outflows:

$$\log N_{\text{HI}} = \log N_{\text{NaI}} + 7.5. \quad (4)$$

This calibration yields a hydrogen column density that is 0.14 dex, or about 30%, smaller than the local calibration by [Rupke](#)

[et al. \(2005\)](#) given in Eq. 2. The discrepancy is not particularly large given the high levels of uncertainty in the assumed values for depletion, ionization correction, and abundance.

4.2. Magnesium

The Mg II doublet ratio, measured for the sum of the velocity components at -47 km/s and -164 km/s, is consistent with unity, indicating strong line saturation since the optically thin value is ~ 2 . We thus use the observed EW to derive a lower limit for the Mg II column density, which we compare to the H I column density for the two velocity components (see Table A.2). This results in an upper limit on the Mg II-to-H I calibration. To further constrain the calibration we also consider the shallower — and thus unsaturated — Mg II absorption features at $v = -428$ km/s and $v = -640$ km/s. In these cases the absorption lines are undetected, and thus yield an upper limit on the column density and a lower limit on the calibration. We discard the $v = -428$ km/s component because the spectrum is affected by strong residuals of unknown origin. For the component at $v = -640$ km/s we measure an upper limit on the EW in the following way. We assume that the Mg II absorption is spectrally unresolved in the FIRE data, which is confirmed by looking at the line widths of UV transitions in the UVES spectra (Figure 4). Given the FIRE spectral resolution $R \sim 6000$, we calculate a line width of 85 km/s, corresponding to 2σ on either side. We then measure the largest fluctuation of the normalized spectrum within the expected line width, and multiply this number by the expected line width (in angstrom) to obtain the upper limit on the EW. This is a conservative measurement that accounts for systematic uncertainties and imperfect normalization of the spectrum, and if some of the observed features are due to genuine Mg II absorption, the true EW would always be lower than our estimated upper limit. We then convert this EW limit to an upper limit on the Mg II column density, which we compare to the H I column density of the velocity component at -640 km/s (see Table A.2).

Analysis of different clumps yielded an upper and a lower limit for the Mg II-to-H I column density ratio. Since the hydrogen column densities of the different clumps are not extremely different, we assume that they have similar conditions, and we combine the upper and lower limits into a relatively small range of values: $6.2 < \log(N_{\text{HI}}/N_{\text{MgII}}) < 6.4$. We can thus obtain an approximate calibration:

$$\log N_{\text{HI}} = \log N_{\text{MgII}} + 6.3. \quad (5)$$

This calibration yields an H I column density that is about an order of magnitude larger compared to the local calibration (Eq. 1) with the standard assumptions, i.e. that most of the Mg atoms are singly ionized, the Mg abundance equals the solar value $\log(n_{\text{Mg}}/n_{\text{H}})_{\odot} = -4.4$, and the dust depletion is $\delta_{\text{Mg}} = -0.8$ ([Savage & Sembach 1996](#); [Jenkins 2009](#); [Wu 2025](#)). Some of the standard assumptions must therefore be substantially incorrect.

We can directly test the degree of ionization of Mg atoms in the absorbing gas using the Mg I transition detected in the FIRE spectrum. We derive a column density for the $v = -47$ km/s component of $\log N_{\text{MgI}} = 12.3$ (see Table A.3), which is at least 30 times smaller than the column density for Mg II, since $\log N_{\text{MgII}} > 13.8$. A small caveat is that the Mg II column density is measured for the blend of the $v = -47$ km/s and $v = -164$ km/s components; however nearly 90% of neutral hydrogen is found in the $v = -47$ km/s component ([Srianand et al. 2008](#)), so that we can safely compare the Mg I and Mg II column densities. We conclude that most of the Mg atoms are

ionized, consistent with local measurements, and that the ionization correction is not the root of the discrepancy between the high-redshift empirical calibration and the local calibration.

Finally, we also provide the Mg I calibration derived empirically from our column density measurements:

$$\log N_{\text{H I}} = \log N_{\text{Mg I}} + 7.8. \quad (6)$$

4.3. Iron

The Fe II 2586, 2600 doublet ratio is 2.0 ± 0.1 , which is substantially lower than the optically thin value of ~ 4 and indicates saturation. We can thus derive a lower limit on the column density of $N_{\text{Fe II}}$, corresponding to an upper limit on the $N_{\text{H I}}/N_{\text{Fe II}}$ calibration (see table A.4). Additionally, the UVES spectrum contains an optically thin Fe II transition (Fe II 1608, shown in Figure 4), which [Noterdaeme et al. \(2008\)](#) use to derive a column density for the main velocity component, $\log N_{\text{Fe II}} = 14.28 \pm 0.05$. We use this value to infer a calibration for Fe II:

$$\log N_{\text{H I}} = \log N_{\text{Fe II}} + 5.8. \quad (7)$$

This calibration yields a neutral hydrogen column density that is 0.4 dex lower compared to the local calibration with the default assumptions for Fe II, i.e., all atoms are singly ionized, $\log(n_{\text{Fe}}/n_{\text{H}})_{\odot} = -4.5$, and $\delta_{\text{Fe}} = -1.7$ ([Savage & Sembach 1996](#); [Jenkins 2009](#); [Wu 2025](#)).

5. Summary and discussion

We have carried out a detailed analysis of a unique system consisting of J1439B, a massive quiescent galaxy at $z = 2.4189$, and a sub-DLA at $z = 2.41837$ ejected by the galaxy, located ~ 38 physical kpc away in projection. The coincidental alignment of this outflow region with a bright background quasar has allowed for a detailed study of the relative abundance of metals and hydrogen in the neutral phase of the outflowing gas.

Our main result was the derivation of empirical relations, given in Eq. 4, 5, 6 and 7, between the metal column densities derived from resonant Na I, Mg II, Mg I and Fe II absorption lines and the hydrogen column density directly measured from Lyman absorption. Our work thus provides an empirical basis for characterizing galactic outflows in the early Universe, a key step toward quantifying the role of feedback in shaping galaxy evolution.

It is instructive to compare our high-redshift empirical calibrations to the ones obtained by plugging local measurements into Eq. 1. We show this comparison in Figure 5 and in Table 1, where we list the commonly adopted values of ionization correction, elemental abundance, and dust depletion. The calibrations based on local measurements yield a hydrogen column density that is 0.14 dex and 0.4 dex higher than our empirical calibrations for Na I and Fe II, respectively; and 1 dex lower for Mg II. This means that the outflow ejected by J1439B has substantially fewer magnesium atoms than one would expect based on local observations. The discrepancy suggests that high-redshift outflows are different from local clumps of neutral gas in one or more properties:

- **Ionization correction:** The ionization correction is expected to depend on the physical properties of the gas, and is particularly uncertain for Na I, which traces a small fraction of Na atoms since they are mostly ionized ([Murray et al. 2007](#); [Baron et al. 2020](#)). However, for Mg we directly confirmed the theoretical expectation that Mg II is much more abundant

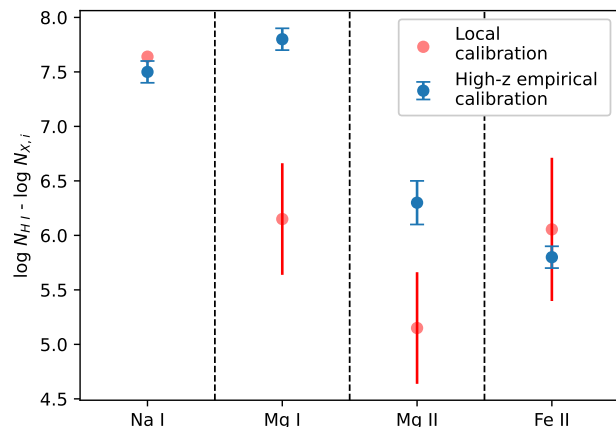


Fig. 5. Column density calibration for different species. The local calibration based on Milky Way gas clouds is shown in red, with the error bar showing the range due to variations in dust depletion. Our empirical calibration derived from J1439B is shown in blue. The two calibrations yield consistent results for Na and Fe, but are inconsistent for Mg, suggesting stronger dust depletion of Mg in high-redshift outflows compared to the Milky Way.

than Mg I. We can thus rule out a strong impact of the ionization correction on the calibration for Mg, and also for Fe which has a similar ionization potential.

- **Elemental abundances:** The gas is often assumed to have solar abundances, but this is not necessarily true since the interstellar medium of high-redshift galaxies is expected to have different chemical abundances compared to the solar neighborhood. Stellar abundance measurements for $z \sim 2$ massive quiescent galaxies find a deficiency in iron, $-0.6 < [\text{Fe}/\text{H}] < 0$, and an enhancement in $[\text{Mg}/\text{Fe}]$, corresponding to roughly solar values of $[\text{Mg}/\text{H}]$ ([Beverage et al. 2024, 2025](#); [Jafariyazani et al. 2025](#)). In one notable case, magnesium is strongly enhanced, $[\text{Mg}/\text{H}] \sim 0.8$ ([Jafariyazani et al. 2020](#)), which would make the discrepancy even worse, since we measure a *lower* Mg column density in J1439B compared to local gas clouds. It is also possible that the abundance of the gas ejected in the outflow is not necessarily representative of that in the galaxy.
- **Dust depletion:** Dust depletion is perhaps the most uncertain ingredient in the local calibration. In Milky Way measurements, the dust depletion of Na shows a large scatter of 0.5 dex ([Wakker & Mathis 2000](#)); while for Mg and Fe the scatter is smaller, but the dust depletion value depends strongly on the gas density, varying by more than 1 dex between different lines of sight ([Jenkins 2009](#); [De Cia et al. 2016](#)). This also means that our assumption of a linear relation between the hydrogen and the metal column densities may not hold, if the dust depletion systematically varies with gas density and, therefore, column density. While the Fe depletion in our system seems consistent with the typical values found in the Milky way (as already noted by [Srianand et al. 2008](#)), the low observed column density of Mg could be explained by a stronger depletion of Mg onto dust grains. This implies dust-to-metal ratios exceeding those observed in the Milky Way or Large Magellanic Cloud ([Roman-Duval et al. 2021](#)) and in local galaxies ([De Vis et al. 2019](#)).

It is thus plausible that the difference between the local calibration and our high-redshift empirical calibration is mostly

	High-z empirical calibration	Local calibration	Ionization correction	Relative abundance	Solar abundance	Dust depletion
	$\log N_{\text{HI}} - \log N_{\text{X},i}$	$\log N_{\text{HI}} - \log N_{\text{X},i}$	$n_{\text{X},i}/n_{\text{X}}$	[X/H]	$\log(n_{\text{X}}/n_{\text{H}})_{\odot}$	δ_{X}
Na I	7.5 ± 0.1	7.6	0.1	0	-5.69	-0.95
Mg I	7.8 ± 0.1	(5.7, 6.7)	0.1	0	-4.38	(-1.27, -0.27)
Mg II	6.3 ± 0.2	(4.7, 5.7)	1	0	-4.38	(-1.27, -0.27)
Fe II	5.8 ± 0.1	(5.4, 6.7)	1	0	-4.46	(-2.24, -0.95)

Table 1. Comparison of our high-redshift empirical calibration to the local calibration, based on Eq. 1. The last four columns list the assumptions used to derive the local calibration. Solar abundance and dust depletion values are taken from [Savage & Sembach \(1996\)](#) for Na and from [Jenkins \(2009\)](#) for Mg and Fe. The ionization correction for Na I is from [Rupke et al. \(2005\)](#), while for Mg I it is estimated from the results of [Murray et al. \(2007\)](#).

due to a strong Mg dust depletion due to a high dust-to-metal ratio. Interestingly, recent theoretical work supports this scenario: using the SIMBA cosmological simulation with a realistic dust model, [Lorenzon et al. \(2025\)](#) find that about 20% of $z \sim 1 - 2$ quiescent galaxies experiencing strong AGN-driven feedback exhibit elevated dust-to-metal ratios compared to local analogues. Such systems may act as reservoirs of large grains that are expelled to CGM distances, where their large size ensures prolonged survival ([Hirashita 2024](#); [Richie et al. 2024](#)). Therefore, strong Mg depletion may naturally result from accretion onto preexisting grains in dense and relatively cool gas. The complexity of the physical processes at play suggests that the conditions of high-redshift outflows differ from those in the local universe.

The most important caveat in our work is that the empirical calibrations have been derived for a single line of sight in only one system. By considering the discrepancy with the local calibrations, and the range of possible values for dust depletion and the other relevant physical properties, we can conclude that our Na I and Fe II calibrations provide at least the correct order of magnitude for the hydrogen column density. Clearly, it is crucial to extend this analysis to a wider sample of outflows in high-redshift massive galaxies, so that the robustness and precision of the calibrations can be assessed.

Despite the large systematic uncertainties still present in the calibrations, our measurements confirm that previous estimates of neutral gas based on resonant metal lines are likely to be correct within an order of magnitude. This is particularly important for the interpretation of recent JWST observations of massive quiescent galaxies at high redshift ([Belli et al. 2024](#); [D'Eugenio et al. 2024](#); [Wu 2025](#)). Our new calibrations confirm that the mass outflow rate in the neutral phase is substantially larger than that of the ionized phase, and it is sufficiently high to deplete the cold gas reservoir on rapid timescales and explain the observed quenching of star formation.

Acknowledgements. SB and AHK are supported by the ERC grant 101076080 “RED CARDINAL”. DD acknowledges support from the NCN through the SONATA grant UMO2020/39/D/ST9/00720 and support from the Polish National Agency for Academic Exchange (Bekker grant BPN/BEK/2024/1/00029/DEC/1). This article includes data gathered with the *Magellan* Telescopes located at Las Campanas Observatory, Chile, as well as observations collected at the European Organisation for Astronomical Research in the Southern Hemisphere under ESO program 278.A-5062(A) and obtained from the ESO Science Archive Facility.

References

Baldwin, J. A., Phillips, M. M., & Terlevich, R. 1981, *PASP*, 93, 5

- Barfety, C., Jolly, J.-B., Förster Schreiber, N. M., et al. 2025, arXiv e-prints, arXiv:2502.13226
- Baron, D., Netzer, H., Davies, R. I., & Xavier Prochaska, J. 2020, *Monthly Notices of the Royal Astronomical Society*, 494, 5396
- Belli, S., Park, M., Davies, R. L., et al. 2024, *Nature*, 630, 54–58
- Beverage, A. G., Kriek, M., Suess, K. A., et al. 2024, *ApJ*, 966, 234
- Beverage, A. G., Slob, M., Kriek, M., et al. 2025, *ApJ*, 979, 249
- Calzetti, D., Armus, L., Bohlin, R. C., et al. 2000, *ApJ*, 533, 682
- Chabrier, G. 2003, *PASP*, 115, 763
- Cicone, C., Brusa, M., Ramos Almeida, C., et al. 2018, *Nature Astronomy*, 2, 176
- Concas, A., Maiolino, R., Curti, M., et al. 2022, *MNRAS*, 513, 2535
- Conroy, C. & Gunn, J. E. 2010, *ApJ*, 712, 833
- Conroy, C., Gunn, J. E., & White, M. 2009, *ApJ*, 699, 486
- Davies, R. L., Belli, S., Park, M., et al. 2024, *Monthly Notices of the Royal Astronomical Society*, 528, 4976–4992
- De Cia, A., Ledoux, C., Mattsson, L., et al. 2016, *A&A*, 596, A97
- De Vis, P., Jones, A., Viaene, S., et al. 2019, *A&A*, 623, A5
- D'Eugenio, F., Pérez-González, P. G., Maiolino, R., et al. 2024, *Nature Astronomy*, 8, 1443
- Draine, B. T. 2011, *Physics of the Interstellar and Intergalactic Medium*
- Förster Schreiber, N. M., Genzel, R., Newman, S. F., et al. 2014, *ApJ*, 787, 38
- Förster Schreiber, N. M. & Wuyts, S. 2020, *ARA&A*, 58, 661
- Gagné, J., Lambrides, E., Faherty, J. K., & Simcoe, R. 2015, *FireHose_v2: Firehose v2.0*
- Harrison, C. M. 2017, *Nature Astronomy*, 1, 0165
- Herrera-Camus, R., Tacconi, L., Genzel, R., et al. 2019, *ApJ*, 871, 37
- Hirashita, H. 2024, *PASJ*, 76, 753
- Jafariyazani, M., Newman, A. B., Mobasher, B., et al. 2025, *ApJ*, 986, 148
- Jafariyazani, M., Newman, A. B., Mobasher, B., et al. 2020, *ApJ*, 897, L42
- Jenkins, E. B. 2009, *ApJ*, 700, 1299
- Johnson, B. D., Leja, J., Conroy, C., & Speagle, J. S. 2021, *ApJ*, 254, 22
- Kennicutt, Jr., R. C. 1998, *ARA&A*, 36, 189
- Kriek, M. & Conroy, C. 2013, *The Astrophysical Journal*, 775, L16
- Kriek, M., van Dokkum, P. G., Labbé, I., et al. 2009, *The Astrophysical Journal*, 700, 221
- Lamperti, I., Harrison, C. M., Mainieri, V., et al. 2021, *A&A*, 654, A90
- Leja, J., Carnall, A. C., Johnson, B. D., Conroy, C., & Speagle, J. S. 2019, *ApJ*, 876, 3
- Leja, J., Speagle, J. S., Ting, Y.-S., et al. 2022, *ApJ*, 936, 165
- Liboni, C., Belli, S., Bugiani, L., et al. 2025, arXiv e-prints, arXiv:2506.05470
- Lorenzon, G., Donevski, D., Lisiecki, K., et al. 2025, *A&A*, 693, A118
- Maltby, D. T., Almaini, O., McLure, R. J., et al. 2019, *MNRAS*, 489, 1139
- Man, A. W. S., Zabl, J., Brammer, G. B., et al. 2021, *ApJ*, 919, 20
- Murray, N., Martin, C. L., Quataert, E., & Thompson, T. A. 2007, *ApJ*, 660, 211
- Noterdaeme, Petitjean, P., Ledoux, C., Srianand, R., & Ivanchik, A. 2008, *Astronomy and Astrophysics*, 491, 397
- Park, M., Belli, S., Conroy, C., et al. 2024, *ApJ*, 976, 72
- Pettini, M., Rix, S. A., Steidel, C. C., et al. 2002, *ApJ*, 569, 742
- Richie, H. M., Schneider, E. E., Abruzzo, M. W., & Torrey, P. 2024, *ApJ*, 974, 81
- Roman-Duval, J., Jenkins, E. B., Tchernyshyov, K., et al. 2021, *ApJ*, 910, 95
- Rudie, G. C., Newman, A. B., & Murphy, M. T. 2017, *The Astrophysical Journal*, 843, 98
- Rupke, D. S., Veilleux, S., & Sanders, D. B. 2002, *ApJ*, 570, 588
- Rupke, D. S., Veilleux, S., & Sanders, D. B. 2005, *The Astrophysical Journal Supplement Series*, 160, 87
- Savage, B. D. & Sembach, K. R. 1996, *ARA&A*, 34, 279

- Shivaei, I., Reddy, N. A., Shapley, A. E., et al. 2015, *The Astrophysical Journal*, 815, 98
- Speagle, J. S. 2020, *MNRAS*, 493, 3132
- Spilker, J. S., Phadke, K. A., Aravena, M., et al. 2020, *ApJ*, 905, 85
- Srianand, Noterdaeme, P., Ledoux, C., & Petitjean, P. 2008, *Astronomy and Astrophysics*, 482, L39
- Steidel, C. C., Erb, D. K., Shapley, A. E., et al. 2010, *ApJ*, 717, 289
- Sun, Y., Ji, Z., Rieke, G. H., et al. 2025, *arXiv e-prints*, arXiv:2504.14682
- Taylor, E., Maltby, D., Almaini, O., et al. 2024, *MNRAS*, 535, 1684
- Tremonti, C. A., Moustakas, J., & Diamond-Stanic, A. M. 2007, *ApJ*, 663, L77
- Vacca, W. D., Cushing, M. C., & Rayner, J. T. 2003, *PASP*, 115, 389
- Valentino, F., Heintz, K. E., Brammer, G., et al. 2025, *arXiv e-prints*, arXiv:2503.01990
- Veilleux, S., Maiolino, R., Bolatto, A. D., & Aalto, S. 2020, *The Astronomy and Astrophysics Review*, 28
- Wakker, B. P. & Mathis, J. S. 2000, *ApJ*, 544, L107
- Wu, P.-F. 2025, *ApJ*, 978, 131

Na I Equivalent Width and Column Density

Component	-47 km/s
EW(Na I 5891)	$(0.85 \pm 0.07) \text{ \AA}$
EW(Na I 5897)	$(0.39 \pm 0.06) \text{ \AA}$
EW ratio	2.2 ± 0.4
$\log(N_{\text{Na I}} / \text{cm}^{-2})$	12.6 ± 0.1
$\log(N_{\text{H I}} / \text{cm}^{-2})^\dagger$	20.1 ± 0.1
$\log(N_{\text{H I}} / N_{\text{Na I}})$	7.5 ± 0.1

Table A.1. Equivalent width and column density measurements of Na I for the component at $v = -47$ km/s. The Na I column density is the average of the values obtained using each of the two transitions.

[†] from [Srianand et al. \(2008\)](#).

Fe II Equivalent Widths and Column Densities

Component	-47 km/s & -164 km/s
EW(Fe II 2586)	$(0.51 \pm 0.03) \text{ \AA}$
EW(Fe II 2600)	$(0.99 \pm 0.03) \text{ \AA}$
EW ratio	2.0 ± 0.1
$\log(N_{\text{Fe II}} / \text{cm}^{-2})$	> 14.0
$\log(N_{\text{H I}} / \text{cm}^{-2})^\dagger$	20.2 ± 0.1
$\log(N_{\text{H I}} / N_{\text{Fe II}})$	< 6.2

Table A.4. Equivalent width of the Fe II transitions for the blend of the components at $v = -47$ km/s and $v = -164$ km/s. The $3\text{-}\sigma$ lower limit on the Fe II column density is derived from the weaker transition (Fe II 2586), which is more constraining.

[†] from [Srianand et al. \(2008\)](#).

Mg II Equivalent Widths and Column Densities

Component	-47 km/s & -164 km/s	-640 km/s
EW(Mg II 2796)	$(1.77 \pm 0.02) \text{ \AA}$	$< 0.54 \text{ \AA}$
EW(Mg II 2803)	$(1.52 \pm 0.02) \text{ \AA}$	$< 0.29 \text{ \AA}$
EW ratio	1.2 ± 0.1	—
$\log(N_{\text{Mg II}} / \text{cm}^{-2})$	> 13.8	< 13.1
$\log(N_{\text{H I}} / \text{cm}^{-2})^\dagger$	20.2 ± 0.1	19.3 ± 0.10
$\log(N_{\text{H I}} / N_{\text{Mg II}})$	< 6.4	> 6.2

Table A.2. Equivalent width of the Mg II transitions and corresponding column densities for different velocity components. The components at $v = -47$ km/s and $v = -164$ km/s are blended and are considered as a single component; the $3\text{-}\sigma$ lower limit on the Mg II column density is derived from the weaker transition (Mg II 2803), which is more constraining. For the undetected component at -640 km/s, the column density is the average of the values obtained using each of the two transitions.

[†] from [Srianand et al. \(2008\)](#).

Mg I Equivalent Width and Column Density

Component	-47 km/s
EW(Mg I 2853)	$(0.28 \pm 0.02) \text{ \AA}$
$\log(N_{\text{Mg I}} / \text{cm}^{-2})$	12.3 ± 0.1
$\log(N_{\text{H I}} / \text{cm}^{-2})^\dagger$	20.1 ± 0.1
$\log(N_{\text{H I}} / N_{\text{Mg I}})$	7.8 ± 0.1

Table A.3. Equivalent width and column density measurements of Mg I for the component at $v = -47$ km/s.

[†] from [Srianand et al. \(2008\)](#).

Appendix A: Measurements

Tables [A.1](#), [A.2](#), [A.3](#), and [A.4](#) report the EW measurements and corresponding column densities for transitions observed in the FIRE spectrum.